Physics in Medicine & Biology

IPEM Institute of Physics and Engineering in Medicine

PAPER • OPEN ACCESS

Characterization of the clinically approved MRI tracer resotran for magnetic particle imaging in a comparison study

To cite this article: Fabian Mohn *et al* 2024 *Phys. Med. Biol.* **69** 135014

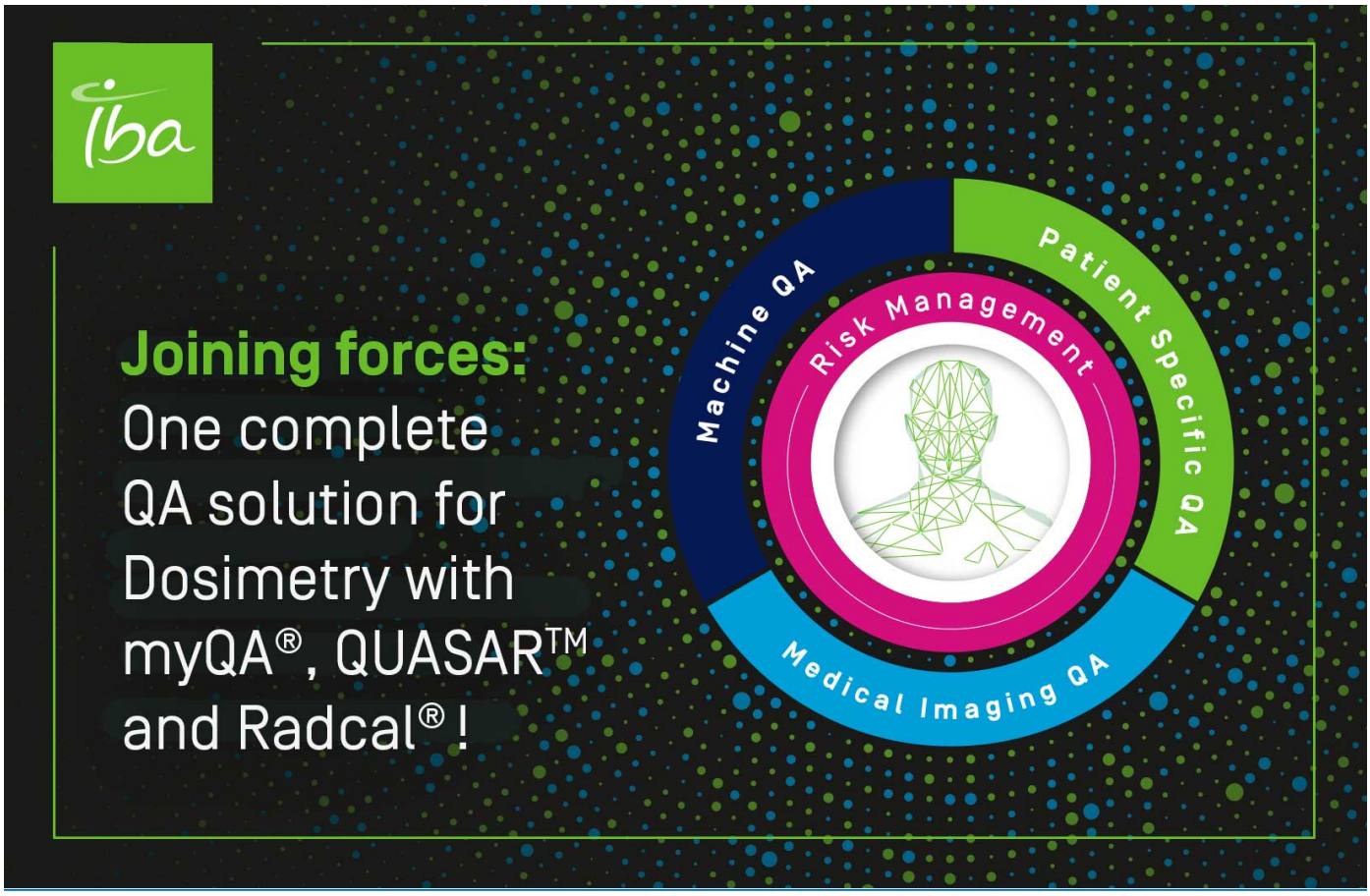

IOP Publishing Phys. Med. Biol. 69 (2024) 135014 https://doi.org/10.1088/1361-6560/ad5828

Physics in Medicine & Biology

IPEM Institute of Physics and Engineering in Medicine

OPEN ACCESS

RECEIVED
9 February 2024

REVISED
21 May 2024

ACCEPTED FOR PUBLICATION
13 June 2024

PUBLISHED
1 July 2024

PAPER

Characterization of the clinically approved MRI tracer resotran for magnetic particle imaging in a comparison study

Fabian Mohn[1,2,*], **Konrad Scheffler**[1,2], **Justin Ackers**[3], **Agnes Weimer**[3,4], **Franz Wegner**[5], **Florian Thieben**[1,2], **Mandy Ahlborg**[3], **Patrick Vogel**[6], **Matthias Graeser**[3,7] and **Tobias Knopp**[1,2,3]

[1] Institute for Biomedical Imaging, Hamburg University of Technology, Hamburg, Germany
[2] Section for Biomedical Imaging, University Medical Center Hamburg-Eppendorf, Hamburg, Germany
[3] Fraunhofer IMTE, Fraunhofer Research Institution for Individualized and Cell-based Medical Engineering, Lübeck, Germany
[4] Institute of Physical Chemistry, University of Hamburg, Hamburg, Germany
[5] Institute for Interventional Radiology, University of Lübeck, Lübeck, Germany
[6] Department of Experimental Physics 5 (Biophysics), University of Würzburg, Würzburg, Germany
[7] Institute of Medical Engineering, University of Lübeck, Lübeck, Germany
[*] Author to whom any correspondence should be addressed.

E-mail: fabian.mohn@tuhh.de

Keywords: MPI, Resovist, ferucarbotran, DLS, VSM, TEM, MPS

Abstract

Objective. The availability of magnetic nanoparticles (MNPs) with medical approval for human intervention is fundamental to the clinical translation of magnetic particle imaging (MPI). In this work, we thoroughly evaluate and compare the magnetic properties of an magnetic resonance imaging (MRI) approved tracer to validate its performance for MPI in future human trials. *Approach.* We analyze whether the recently approved MRI tracer Resotran is suitable for MPI. In addition, we compare Resotran with the previously approved and extensively studied tracer Resovist, with Ferrotran, which is currently in a clinical phase III study, and with the tailored MPI tracer Perimag. *Main results.* Initial magnetic particle spectroscopy (MPS) measurements indicate that Resotran exhibits performance characteristics akin to Resovist, but below Perimag. We provide data on four different tracers using dynamic light scattering, transmission electron microscopy, vibrating sample magnetometry measurements, MPS to derive hysteresis, point spread functions, and a serial dilution, as well as system matrix based MPI measurements on a preclinical scanner (Bruker 25/20 FF), including reconstructed images. *Significance.* Numerous approved MNPs used as tracers in MRI lack the necessary magnetic properties essential for robust signal generation in MPI. The process of obtaining medical approval for dedicated MPI tracers optimized for signal performance is an arduous and costly endeavor, often only justifiable for companies with a well-defined clinical business case. Resotran is an approved tracer that has become available in Europe for MRI. In this work, we study the eligibility of Resotran for MPI in an effort to pave the way for human MPI trials.

1. Introduction

Magnetic particle imaging (MPI) is an emerging tomographic technique that combines high magnetic nanoparticle (MNP) sensitivity with high temporal and spatial resolution (Gleich and Weizenecker 2005). The main principle is the exploitation of the nonlinear magnetization behavior of MNPs in a periodic magnetic excitation field (drive field). A spatial resolution is achieved by using a magnetic gradient field (selection field) keeping the MNPs in saturation everywhere except in a small field-free-region. As a promising tomographic technique without ionizing radiation, MPI has high potential in numerous medical applications. Due to its very high temporal resolution, a main focus is cardiovascular and periinterventional imaging (Weizenecker *et al* 2009, Haegele *et al* 2012, 2016a, 2016b, Bakenecker *et al* 2018, Herz *et al* 2019, Wegner 2021) as well as perfusion imaging (Ludewig 2017, Kaul *et al* 2018, Mohn *et al* 2023). Due to the multifaceted properties of MNPs that can be exploited by MPI, further applications are part of extensive

research: development of dedicated MPI instruments for treatment of vascular stenosis (Ahlborg 2022), cellular tracking (Zheng *et al* 2015, Sehl *et al* 2020, Remmo *et al* 2022), local magnetic hyperthermia (e.g. tumor imaging and therapy without surgery) (Chandrasekharan 2020, He *et al* 2023) and navigation of magnetic micro-robots for targeted drug delivery and treatment of cerebral aneurysms (Bakenecker *et al* 2021, Bui *et al* 2021, 2023). The authors refer to reviews for detailed insight on the full functionality of MPI as well as the progress made from the first prototype in 2005 to the first commercial preclinical systems, given by Knopp *et al* (2017). Further outlines over current research and applications can be found in Billings *et al* (2021), Neumann (2022), Yang *et al* (2022).

Besides upscaling MPI hardware to human-sized scanners (Sattel *et al* 2015, Mason *et al* 2017, Rahmer *et al* 2018, Graeser 2019, Vogel *et al* 2023) and addressing safety concerns (Saritas *et al* 2013, Schmale 2013, Thieben *et al* 2024), the availability of suitable MNPs with medical approval is crucial for a clinical translation of MPI. The development of medical MNPs is primarily driven for the application in magnetic resonance imaging (MRI). Unfortunately, most MNPs developed for MRI do not have the specific magnetic properties that are needed to generate a strong signal in MPI. If nanoparticles are too small, the thermal energy dominates the magnetic energy, inducing a rather linear magnetization behavior. Thus, they are not suited for MPI, where signal generation and spatial encoding is based upon a nonlinear magnetization. On the other hand, if particles are too large, they block the Néel relaxation process due to strong magnetic anisotropies. This reduces their ability to follow the magnetic field at excitation frequencies between 10 kHz to 150 kHz (Deissler *et al* 2014, Tay *et al* 2017). An important MRI MNP that has magnetic properties suitable for MPI is ferucarbotran, namely Resovist, formerly with medical approval in Germany (Bayer Schering Pharma, Berlin, Germany) and still approved in Japan (I'rom Pharmaceuticals, Tokyo, Japan). However, due to a wide particle size distribution with the majority of particles being smaller than 15 nm, only a small fraction of the total iron mass contributes to a useful MPI signal (Yoshida *et al* 2013). First dedicated MNPs, tailored to enhance the MPI specific performance, were published by Ferguson *et al* (2009). Later, a monodisperse iron core MNP coated with polyethylene glycol (Ferguson 2015), evolving into the formerly commercially available MNPs LS-008 (LodeSpin Labs, Seattle, USA) was developed. In 2013, dextran coated multicore magnetic iron oxide nanoparticles were presented by Eberbeck *et al* (2013), commercially available as the preclinical MNPs Perimag and Synomag (micromod Partikeltechnologie, Rostock, Germany). The mean magnetic core size of Perimag is about 19 nm, in the range where a coupled Brownian and Néel relaxation occurs (Eberbeck *et al* 2013, Ludwig *et al* 2013). Moreover, MNPs can also undergo a system-specific optimization, i.e. to match a particular type of excitation: the formation of particle chains has improved the nonlinear response in 1D excitation (Tay 2021). A comparison of commercial MNPs with respect to their MPI performance is given by Lüdtke-Buzug *et al* (2013) and Ludwig *et al* (2013) and more recently by Irfan *et al* (2021a). A recent overview of the development of MPI tailored MNPs is given by Harvell-Smith *et al* (2022).

The research on MPI tailored tracers increased in the last years (Antonelli *et al* 2020, Liu *et al* 2021, Moor *et al* 2022, Thieben *et al* 2023a), however, none of these tracers has reached a level of development that would warrant the costs of a medical approval and consequently their use in clinical MPI remains distant. Such an approval requires a well-defined business case and a long-term market to justify the multi-annual process and investment in a new approval. Fortunately, Resotran (b.e.imaging GmbH, Baden–Baden, Germany; medical approval granted in Oct. 2022 under reg. no. 7002 837.00.00 in Germany), containing ferucarbotran MNPs, has recently received approval in certain countries, including Germany and Sweden. Additionally, there is a phase III clinical trial underway for ferumoxtran MNPs called Ferrotran, consisting of ultrasmall superparamagnetic iron-oxide nanoparticles (USPIONs). Both MNPs are officially authorized for MRI liver imaging and initial measurements showed similar MPI performance (Hartung *et al* 2023, Scheffler *et al* 2023). General concerns regarding toxicity of MNPs in long-term metabolism remain (Sun *et al* 2008, Billings *et al* 2021, Rubia-Rodríguez 2021), although the incidence of adverse events for ferucarbotran (Resovist) is low with 7.1% (Wang 2011). The performance of known ferucarbotran-based tracers such as Resovist and VivoTrax (Magnetic Insight Inc. Alameda, USA) is similar (Song *et al* 2018, Gevaert *et al* 2022, Yeo *et al* 2022). A comparison of VivoTrax and Perimag is found in Irfan *et al* (2021b), Synomag is also included by Yeo *et al* (2022), and Synomag, Perimag, and Resovist are compared in Ludewig (2022).

The purpose of this paper is to provide a comprehensive characterization of the MNPs Resotran and Ferrotran with a focus on their applicability to MPI. Comparisons will be made with the extensively studied MRI MNPs Resovist as well as with the MPI tailored MNPs Perimag. We chose Perimag because of its established position and its appearance in a wide range of publications and open datasets (Knopp *et al* 2020). In this work, we address the characterization of the four MNPs Perimag, Resotran, Resovist and Ferrotran by transmission electron microscopy (TEM), dynamic light scattering (DLS), vibrating sample magnetometry (VSM) and magnetic particle spectroscopy (MPS) measurements. In addition, 2D MPI reconstructions for

two different phantoms are compared at the system matrix level and in the image domain for future applications in MPI. We present and discuss the results of applying these methods to all four MNPs.

2. Materials and methods

For a comprehensive characterization of the four MNPs Perimag, Resotran, Resovist and Ferrotran regarding their suitability in MPI, we analyze shape parameters, magnetic properties, system matrix performance and image reconstructions.

First, the hydrodynamic diameter can be determined using DLS and the core diameter of the magnetite can be determined using TEM. The latter provides a detailed visualization of the inner iron core in a sub-nanometer resolution and thus of the relationship between the iron structure and performance in MPI. Second, regarding the magnetic properties, we determine the static magnetization characteristic by VSM and the dynamic particle response to a drive field by MPS. The VSM data are used to observe the MNPs in the saturation region as well as their nonlinear slope through the origin according to the Langevin model. MPS measurements show the particle spectrum and can reveal relaxation induced hysteresis as a function of excitation amplitude. We also measure a dilution series and different offset-field combinations to plot two types of point spread functions (PSFs) that can be used to estimate image resolution. Third, prior to reconstruction, the signal-to-noise ratio (SNR) and system matrix patterns are analyzed to estimate the performance and compare Resotran to Resovist in the frequency domain. The fineness of the frequency pattern indicates the expected resolution of the reconstructed image. Finally, the MNPs are evaluated in a typical MPI imaging scenario to demonstrate suitability and resolution for medical imaging, using a commercial imaging system (Bruker MPI 25/20 FF). Two different phantoms are measured and we also perform cross reconstructions using the Resotran system matrix to reconstruct all other tracers to assess compatibility. In the following we introduce each of these methods in detail and describe the performed experiments and their implications.

2.1. MNP material

The MNPs are measured at a concentration of $8.5\,\mathrm{mg_{Fe}\,ml^{-1}} \approx 152\,\mathrm{mmol\,l^{-1}}$, a threshold that is chosen to avoid concentration dependent behavior (Löwa *et al* 2016). For Perimag, we use stock dispersion with this concentration (LOT 045 211). Both Resotran (LOT F1901) and Resovist (LOT 20F01) are supplied with $28\,\mathrm{mg_{Fe}\,ml^{-1}}$ and are therefore diluted with distilled water. Ferrotran (LOT PRX19L02) is shipped as freeze-dried powder and has a concentration of $20\,\mathrm{mg_{Fe}\,ml^{-1}}$ once dispersed in water, which we dilute to the same level of $8.5\,\mathrm{mg_{Fe}\,ml^{-1}}$. All MNPs are made from iron oxide and coated with a dextran shell. More specifically, Resovist and Resotran are made from ferucarbotran and Ferrotran is made from ferumoxtran-10 lyophilisate and additionally coated with sodium citrate.

2.2. DLS

The hydrodynamic diameter of the aqueous iron oxide nanoparticle dispersion is measured using DLS on a Zetasizer Pro-Blue (Malvern Panalytical Ltd, Malvern, United Kingdom) device at a laser wavelength of 633 nm. The sample is diluted 1:100 with Milli-Q (Merck Group, Darmstadt, Germany) water and measured in a plastic cuvette at an optical path length of 1 cm. Each measurement is recorded over three cycles (3 averages) of 30 s each and an intensity weighted mean hydrodynamic diameter of the particle ensemble (z-average) is calculated with the respective polydispersity index (PDI). The z-average is based on the method of cumulants (Koppel 1972), where the monochromatic light source is scattered by the MNPs in suspensions and the light intensity of the interference pattern is evaluated for a logarithmic normal size distribution (Thomas 1987). The light scattering is caused by the particle ensemble surface and the results include the dextran shell, therefore a size distribution of the hydrodynamic diameter is shown, not the magnetite core. The data is analyzed using the ZS XPLORER software version 3.2.0.84 (Malvern Panalytical Ltd, Malvern, United Kingdom).

2.3. TEM

TEM measurements are performed with a JEOL JEM-1011 (JEOL Ltd, Tokyo, Japan) at 100 kV equipped with two spherical aberration correction devices (CETCOR and CESCOR by CEOS GmbH, Heidelberg, Germany) and a Gatan 4K UltraScan 1000 (Gatan Inc., Pleasanton, USA) camera. For the preparation, 10 μl of the diluted nanoparticle dispersion are placed on a carbon-coated TEM copper slide with a 400 mm mesh. The excess solvent is removed with a filter paper and the TEM grid is air-dried. The recorded images achieve a $2 \cdot 10^5$-fold magnification at 100 kV. For a quantitative analysis, the size of 250 individual particles is measured using the software ImageJ (NIH, Bethesda, USA) and plotted in a histogram to visualize the size-distribution, following the guidelines of (2014) for counting (Pyrz and Buttrey 2008). Our evaluation

only accounts for the short-axis diameter (Pyrz and Buttrey 2008, Verleysen *et al* 2019) of individual particles and we do not count any particle clusters or chains (Bender 2018, Bresch *et al* 2022).

2.4. VSM

The magnetization of the liquid samples in response to static magnetic fields are characterized using a VSM (Lakeshore 8607 VSM, Westerville, USA). A quantity of 20 μl is filled into the sample holder and covered with oil, resulting in an almost spherical sample shape. A sweep of the external magnetic field in the range of ± 2 T (step size 20 mT) and in the range of ± 30 mT (step size 0.5 mT) is performed. The signal is averaged for 1 s at each step. The results are given in the domain of the magnetic moment, calibrated by the VSM (Foner 1959) and divided by 2 to match the iron mass of the MPS samples of 85 μg_{Fe} (10 μl). Direct measurement of 10 μl would have been possible, but accurately pipetting amounts below 20 μl into the VSM sample holder proved more error prone than measuring the larger sample and relying on the linear signal response (Knopp *et al* 2017) (refer to the dilution series of section 3.4).

2.5. MPS

We use an arbitrary waveform MPS to measure different 10 μl samples of MNPs exposed to a combination of a static and a dynamic magnetic field (Mohn *et al* 2022). These fields are homogeneous inside the measurement chamber and consist of two quantities, a sinusoidal drive-field B_{drive} at 26.042 kHz and a static offset field B_{offset} for saturation. In this case, both fields are oriented in the same direction. A set of static offsets in the range of ± 30 mT (step size 0.5 mT) is measured for different drive-field amplitudes in the range of 4 to 20 mT (step size 2 mT). All measurements are averaged over 45 drive-field periods (1.73 ms) to reduce noise at low drive-field values. The receive bandwidth of the MPS device is 7.8125 MHz, using a stack of two RedPitaya STEMlab 125-14 and the open source software stack composed of RedPitayaDAQServer (Hackelberg *et al* 2022) and MPIMeasurements.jl (Hackelberg *et al* 2023). The system is calibrated using a transfer function measured with a small calibration coil (Thieben *et al* 2023b). By calibrating the entire receive chain, we can express the particle response in terms of the net magnetic moment m and thus obtain device-independent measurements that are particle specific. The hysteresis curve is obtained by plotting m against the actual drive-field B_{drive}, using the calibrated reference channel in mT of the device.

2.5.1. PSF

Two types of PSFs are calculated to visualize tracer differences using the MPS data. A narrow and steep PSF is generally indicative for high resolution MPI (Croft *et al* 2012), while relaxation effects cause asymmetries and broadening of the PSF. The dynamic PSF is based on a straight forward approach by plotting one half-cycle of $\frac{\mathrm{d}m}{\mathrm{d}t}$ against the excitation B_{drive} (positive half-cycle only). Consequently, the PSF approaches a zero-crossing at the maximum amplitude of B_{drive}. The calculation of the x-space PSF is typically based on partial field-of-views (FOVs) and a DC-recovery step (Goodwill *et al* 2012, Lu *et al* 2013), which becomes obsolete when the fundamental is not filtered, i.e. when using a gradiometric arbitrary waveform MPS, as validated by Tay *et al* (2016). To this end, we plot the value of $\frac{\mathrm{d}m}{\mathrm{d}t}$ at the maximum field gradient of B_{drive} against each offset step value. The data is then normalized to facilitate the comparison of the full width at half maximum (FWHM) of the x-space PSF.

2.5.2. Serial dilution

To investigate the linearity between the particle magnetization and the total amount of iron in a sample, we perform a dilution series with an MPS with 1D sinusoidal excitation with 20 mT at 26.042 kHz. Each measurement is performed using 10 background frames and 10 foreground frames, using a transfer function correction and a sample of 10 μl of each MNP. Starting with 8.5 $\mathrm{mg_{Fe}\,ml^{-1}}$ the concentration is halved seven times, dispersed with the same amount of distilled water, leading to a set of 8 measurements per tracer with $8.5 \cdot \left(1/2\right)^i \mathrm{mg_{Fe}\,ml^{-1}}$ for $i = 0, \ldots, 7$. Despite working with highest precision, potential inaccuracies while pipetting increase with a diminishing total iron amount. We evaluate the absolute values of the third harmonic of the measured magnetization response in the frequency domain (Löwa *et al* 2020) to compare the results of the 4 different MNPs.

2.6. MPI

MPI is performed using the preclinical Bruker MPI system 25/20 FF. We use a 2D Lissajous excitation in xy-direction with an amplitude of 12 mT at a frequency of 24.509 kHz/26.041 kHz in x-/y-direction and a selection field gradient of $(-1, -1, 2)$ T m^{-1} generating a FOV of 24×24 mm^2. All measurements are taken with a dedicated 3D receive coil with an open bore of 72 mm, based on the gradiometric approach, a custom built low noise amplifier, and corrected with a measured transfer function (Graeser *et al* 2017). The 2D system matrices are measured using a delta-sample of $1 \times 1 \times 5$ mm^3 filled with 4 μl of each tracer diluted to

a common iron concentration of 8.5 $mg_{Fe}\,ml^{-1}$ on $29 \times 29 \times 1$ equidistant grid positions covering $29 \times 29 \times 5\,mm^3$. A quantitative comparison of the different MNPs on system matrix level is done by considering the SNR profiles and characteristics (Franke *et al* 2016) as well as the structural similarity index measure (SSIM) (Wang *et al* 2004) over all frequency components. Furthermore, a qualitative comparison is given on three selected frequency components with high (99.57 kHz), medium (104.17 kHz), and low (108.76 kHz) SNR.

The MPI reconstructions are performed on two different phantoms, each measured with 500 averages (10 s measurement time). The first phantom consists of three $1 \times 1 \times 1\,mm^3$ square samples, filled with 0.8 μl of the tracer at 8.5 $mg_{Fe}\,ml^{-1}$, placed in the corners of an equilateral triangle with an edge length of 9.24 mm. If the MNPs are MPI suitable, the individual dots should be easily separable. The second phantom is more complex and consists of a spiral with two full windings. The round vessel phantom consists of windings with an inner diameter of 2.5 mm, separated by an edge-to-edge distance of 2.8 mm. It is filled with a concentration of 8.5 $mg_{Fe}\,ml^{-1}$. Although the total iron amount is much higher than in the three-dot phantom, a complete resolution of the spiral is expected to be more challenging than for the three-dot phantom. Image reconstruction is performed using the iterative Kaczmarz method and a careful selection of frequency components and regularization strength for each individual image. Complete fairness in the comparison is a hard problem due to its complexity and is currently part of research (Weizenecker *et al* 2007, Dittmer *et al* 2021, Hackelberg *et al* 2024, Scheffler *et al* 2024).

3. Results

All measurements of section 2 were performed identically for the four considered MNPs. With the exception of the dilution series and the DLS experiments, all MNPs were prepared at identical concentrations of 8.5 $mg_{Fe}\,ml^{-1}$ (152 $mmol\,l^{-1}$).

3.1. DLS

Results of the DLS measurements are shown in figure 1. Light intensity is given in percent for each size bin (round marks) with respect to all measured bins of the log normal size distribution. Perimag exhibits the largest hydrodynamic sizes with a peak value at 114 nm (z-average 102.5 nm, PDI 0.1853), followed by Resotran with a narrower distribution and a peak at 74 nm (z-average 66.32 nm, PDI 0.1806). Resovist is roughly comparable to Resotran, with a peak value at 65 nm (z-average 55.97 nm, PDI 0.2007). Ferrotran is a ultra-small superparamagnetic iron oxide (USPIO) and has a hydrodynamic diameter of around 28 nm (z-average 27.82 nm, PDI 0.09) and the narrowest distribution of all tracers.

3.2. Transmission emission microscopy

In figure 2, TEM images and a histogram of individual particles for a count of $n = 250$ short-axis core diameter measurements are shown for each tracer. The mean μ and the standard deviation σ are given in the top right corners. TEM images provide indications of shape, structure, size and uniformity of the nanoparticles. Note that the counting rule applied significantly influences the classification (Bresch *et al* 2022), but we mostly observe spherical individual particles without strong elongation and do not classify particle clusters.

Perimag and Ferrotran exhibit the smallest mean core diameter, followed by Resotran and Resovist in increasing order. As TEM images show the magnetite cores, clusters and particle-chains are visible as well as overlapping particles. Especially for Perimag, such clusters and chains are visible in the pictures and the cores tend to form large clusters in the range of 20 to 50 nm. Visual inspection of Resotran and Resovist indicates a similar structure and size of both tracers. Ferrotran shows isolated cores, separated by their ligand hull, which reduces magnetic interaction in between particles. Seemingly, no clusters are formed and particles do not overlap, which agrees with DLS results for this USPIO.

3.3. VSM

The results of the VSM measurements are shown in figure 3. All particle samples show the expected superparamagnetic behavior with sigmoidal magnetization curves and no detectable hysteresis. In the ± 2 T range plot, the magnetization curves of Resovist and Resotran are very similar, reaching almost the same saturation magnetization at about 83.6 $Am^2\,kg_{Fe}{}^{-1}$. The saturation magnetization of Perimag is around 89.3 $Am^2\,kg_{Fe}{}^{-1}$. Ferrotran has the highest saturation magnetization of the investigated particles (93.88 $Am^2\,kg_{Fe}{}^{-1}$), but has a much lower initial slope with an almost linear curve in the MPI relevant range ± 30 mT, when the origin of the left plot in figure 3 is considered. In contrast, Perimag shows the strongest nonlinearity with an initial slope around 1.23 $\mu Am^2\,mT^{-1}$, whereas Resotran exhibits 0.67 $\mu Am^2\,mT^{-1}$ and Resovist is lower with 0.45 $\mu Am^2\,mT^{-1}$ (evaluated at ± 1 mT).

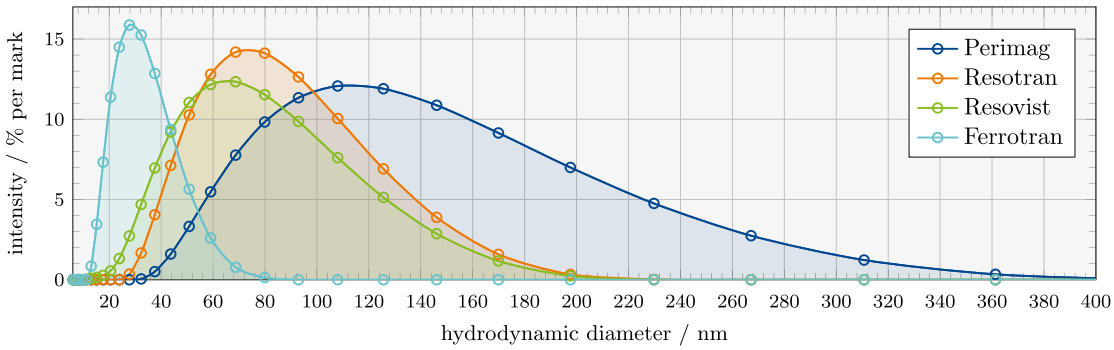

Figure 1. Intensity weighted log normal size distribution by DLS. A sample with a 1:100 dilution of each tracer was measured using DLS to determine the hydrodynamic particle diameter, that includes the dextran shell coating (laser wavelength of 633 nm, 30 s measurement time, 3 averages).

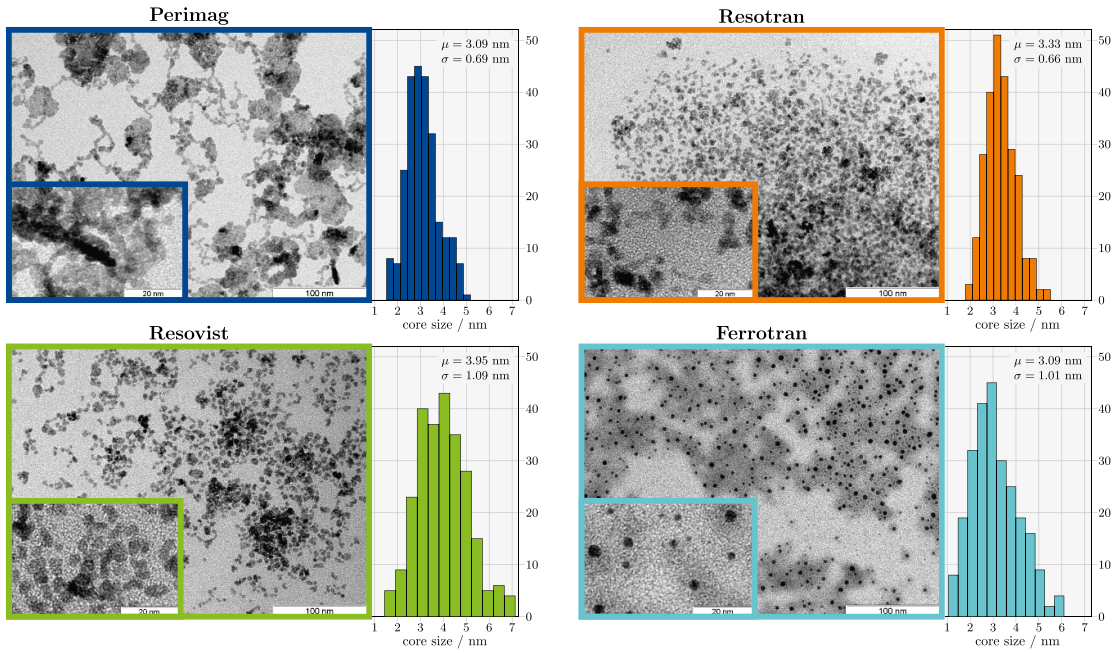

Figure 2. TEM images. Samples of each tracer as visualized by TEM for two different zoom levels at 20 nm and 100 nm reference scale, showing the iron-oxide core. Each histogram lists the mean μ and the standard deviation σ of the core short-axis diameter for a count of $n = 250$ particles categorized into 12 individual size bins. Note, that Perimag, Resotran and Resovist form clusters and chains, which were not counted, whereas Ferrotran accounts for the smallest and individual particles (USPIOs).

3.4. MPS

Four types of plots are generated in figure 4, each containing measurements of the four MNPs under investigation. On the top, the spectrum for 6 mT and 20 mT excitation amplitude is shown, because these amplitudes refer to a realistic range for human-sized MPI (Ozaslan *et al* 2022, Thieben *et al* 2024). We only plotted the odd harmonics, because they contain the majority of the information on the nonlinear magnetization of MNPs in a homogeneous sinusoidal excitation field (without offset fields). The spectrum of Resotran and Resovist are very similar for both 6 mT and 20 mT, the amplitude of Resotran being slightly higher in the range of 5%–15%. Compared to Resotran, Perimag has a 1.5–2.0 fold higher signal amplitude at low harmonic indices, increasing to 2.5 at higher indices above 400 kHz. Ferrotran has an overall low signal amplitude, as already indicated by the linear slope in figure 3. Even at 20 mT excitation, useful signal is only detectable below 300 kHz, indicating insufficient MPI signal.

In the middle row, the hysteresis curve is plotted, which shows a residual magnetization for all tracers, except for Ferrotran, which does not seem to undergo a measurable, relaxation-induced hysteresis. On the bottom the different normalized PSFs are plotted. We state the FWHM for the x-space PSF to facilitate comparison. At 6 mT, all tracers except Ferrotran indicate very similar magnetic properties, however, the difference in terms of FWHM between both PSF types are large. This effect reduces at 20 mT with a trend for the x-space PSF to broaden and the dynamic PSF to narrow. The PSFs show that the relaxation behavior of

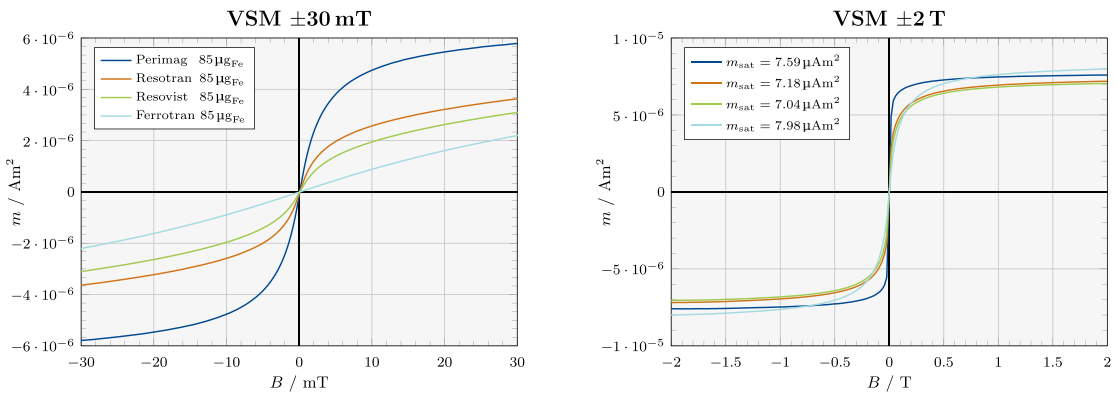

Figure 3. VSM results. The magnetic moment is plotted against the external field for two different ranges with identical samples. The steeper the slope of the net magnetic moment m at the origin, the stronger is the nonlinear response which is the useful signal in MPI.

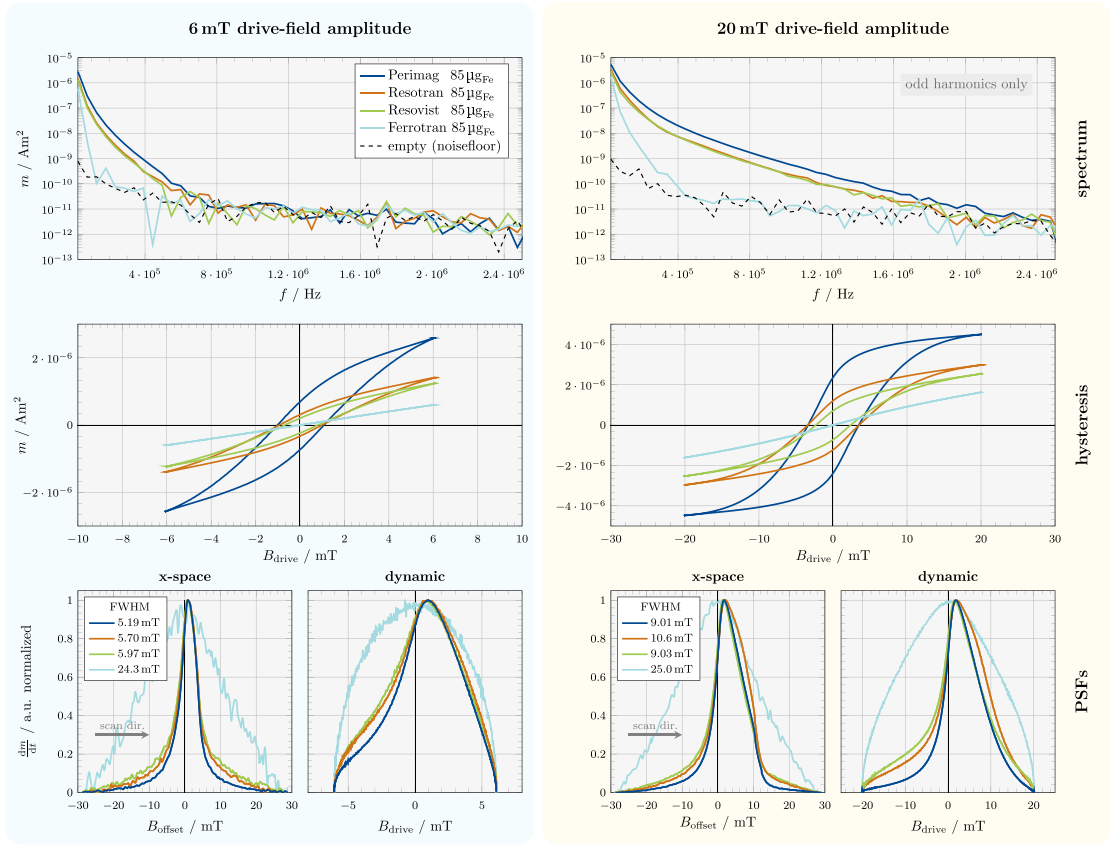

Figure 4. Arbitrary waveform MPS results. Spectrum, hysteresis and PSFs from top to bottom for 6 mT and 20 mT sinusoidal drive-field excitation. The frequency spectrum only contains odd harmonics of the fundamental $f_1 = 26.042\,\mathrm{kHz}$. The FWHM of the x-space PSF is given in the legend and the gray arrow indicates the scan direction (positive half-wave).

the first three tracers is very similar, especially at low excitation amplitudes. At 20 mT the measured Resotran sample seems to broaden slightly, possibly due to a stronger Brownian component. Both PSFs indicate an inferior MPI image quality for Ferrotran. The noisy shape is caused by the normalization, which maps all peak amplitudes to one. Their original relation of maximum signal can be deduced from the saturation region of the hysteresis curve above.

In a deeper MPS analysis, we refer to three different types of plots in figure 5. On the left side, the results of the MPS dilution series are shown. We observe a linear behavior in the absolute magnitude of the third harmonic over all concentrations down to $8.5 \cdot \left(1/2\right)^7 \approx 0.066\,\mathrm{mg\,ml^{-1}}$ for Perimag, Resotran and Resovist. While Perimag produces the highest signal, the results indicate that Resotran and Resovist are relatively comparable in signal strength, with Resotran's signal being slightly higher. Ferrotran gives a much weaker

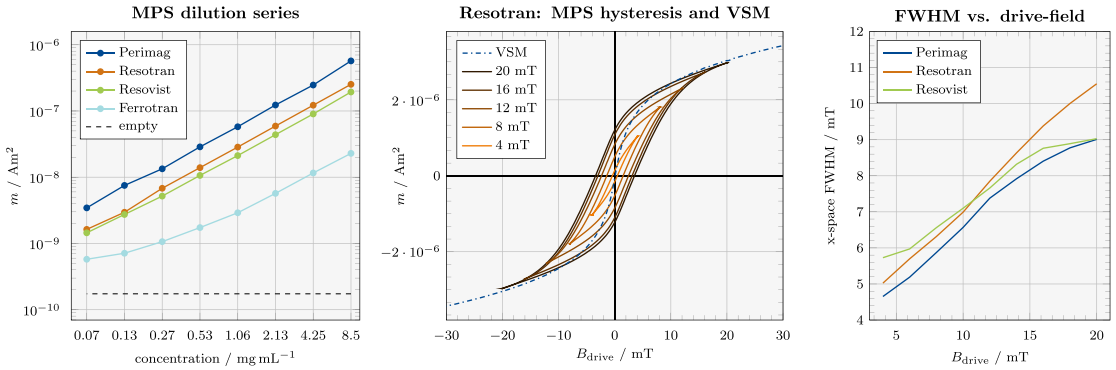

Figure 5. MPS data analysis. On the left, a dilution series of all tracers is shown. The absolute value of the third harmonic of exponentially decreasing concentrations between $8.5 \cdot \left(1/2\right)^{0}$ mg ml^{-1} and $8.5 \cdot \left(1/2\right)^{7}$ mg ml^{-1} is plotted (20 mT, 26.042 kHz). The center plot focuses on Resotran: the hysteresis for 5 different excitation amplitudes is plotted (bright to dark for increasing amplitude) with an overlay of the VSM curve (dash-dot). On the right, the FWHM is plotted against the drive-field amplitude. Ferrotran was omitted to retain a detailed scale.

MPS signal, starting with a linear result for higher concentrations, but loosing linearity by the 4th dilution step towards lower concentrations. At the lowest two concentrations, the response is barely higher than the background signal.

In the center of figure 5, the hysteresis curve for Resotran is plotted in a range of 4 to 20 mT with 4 mT steps for the excitation fields. In addition, the VSM curve of Resotran is overlaid, as obtained from figure 3. The hysteresis broadens with increasing amplitude and the turning point in saturation (maximum/minimum of B_{drive}) seems to approach the VSM line at high amplitudes.

The x-space PSF was evaluated at varying excitation amplitudes between 4–20 mT in 2 mT intervals, as shown on the right-hand side of figure 5. The resulting plot displays the FWHM of the PSFs against the drive-field amplitude and provides detailed insights into its tendency to increase with amplitude, which was previously observed in figure 4. Specifically, the FWHM seems to increase linearly with amplitude. However, the linear increase is only applicable to a small region, and both Perimag and Resovist demonstrate a decline above 16 mT. On the other hand, Resotran maintains a consistent linear pattern throughout our measurement range.

3.5. MPI

For a quantitative comparison of the system matrices, we consider the SNR profile of the x-channel as well as an SSIM comparison with Resotran over all frequencies of the x-channel, shown in the upper part of figure 6. As expected, Perimag achieves the highest SNR over the entire frequency band. Especially for higher harmonics above 350 kHz the measured signal outperforms the other tracers. Ferrotran clearly shows the lowest SNR profile. Only the first 4 harmonics reach SNR levels suitable for MPI. In contrast, Resotran and Resovist achieve SNR profiles suitable for good MPI measurements with useful frequency components up to 500 kHz. Higher harmonics show good SNR levels above 10 up to 350 kHz. Overall, Resotran and Resovist show very similar SNR profiles. This is supported by the SSIM comparison in the 3rd row of figure 6. Moreover, the SSIM indicates, that the Resotran and Resovist system matrix patterns are similar in structure. Especially around the harmonics with a SNR above 10, the SSIM is high and the system matrix patterns of Resotran and Resovist are very similar. We also considered mean absolute error and mean squared error between the different spectra and the Resotran spectrum, but the results are very similar to the SSIM course and we decided to focus on the SSIM to reduce redundant information.

A qualitative comparison of the system matrices on three selected frequency components with high SNR (99.57 kHz), medium SNR (104.76 kHz) and low SNR (108.76 kHz) is displayed in the bottom part of figure 6, which are sidebands of the fourth harmonic. The fourth harmonic was selected for analysis, because it has a higher SNR than the third on the Bruker MPI 20/25 FF, in part due to our custom receive chain without harmonic notching (Mattingly *et al* 2022). The close resemblance of the system matrix components of Resotran and Resovist can be seen in phase and amplitude. Moreover, the wave patterns show the same structure when compared to Perimag. Visible differences compared to Perimag can be seen in the component with medium SNR, especially in the outer corners and in the component with low SNR, where Resotran and especially Resovist have significantly more noise. At the highest frequency we also see Resotran and Resovist differing in quality. The system matrix components of Ferrotran are clearly different and the wave patterns

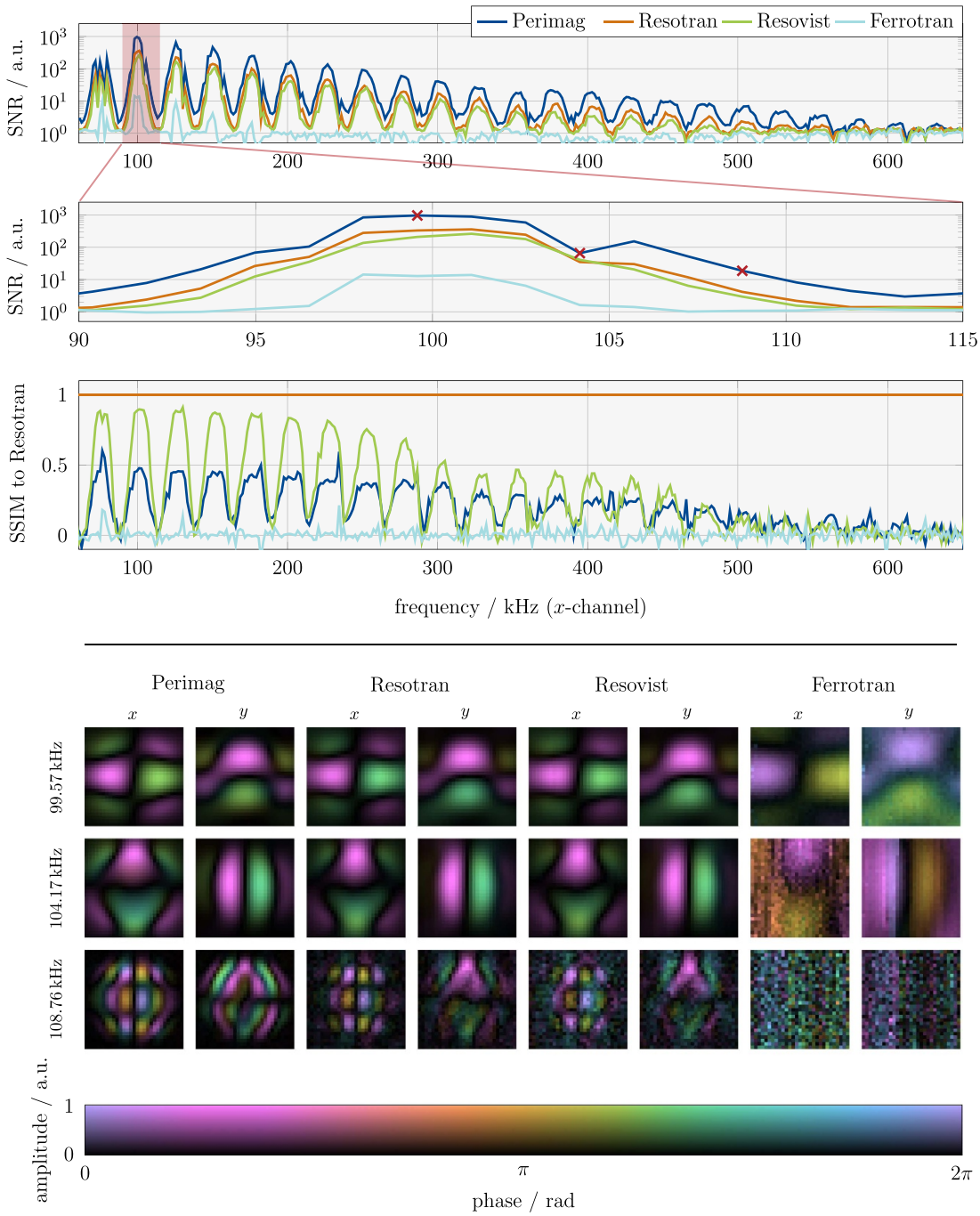

Figure 6. MPI system matrices. On the top, the SNR of the *x*-channel of all MNPs is shown, as measured with the preclinical system Bruker MPI 20/25 FF with *xy*-excitation. The relation of signal amplitudes and visible harmonics is similar to the MPS measurements. The second row shows a zoom on the fourth harmonic including its sidebands, from 90 to 115 kHz. The third row displays the SSIM of Perimag, Resovist and Ferrotran with respect to Resotran for the full spectrum. Below, the complex color-coded system matrix pattern are shown for three frequencies (marked by red crosses above) across all tracers.

are not represented correctly even for the component with the high SNR value. Phase and amplitude are also different and noise is clearly dominant.

Lastly, we consider the reconstruction results of two phantoms, a 3-dot phantom and a spiral phantom, given in figure 7. In the upper part, reconstructions with the dedicated system matrices are shown. In the lower part, cross-reconstructions with the Resotran system matrix are shown for all other tracers. The SSIM to the reconstruction result of Resotran is superposed in the lower right corner for all reconstructions.

The images indicate, that both phantoms can be reconstructed successfully by using Perimag, Resotran and Resovist. Here, Perimag visibly achieves the best image quality, followed by Resotran. Ferrotran is not able to resolve the phantoms at all. Cross-reconstructions using the Resotran system matrix are possible for Perimag and Resovist on both phantoms. While the result for Perimag gets worse, the reconstruction result

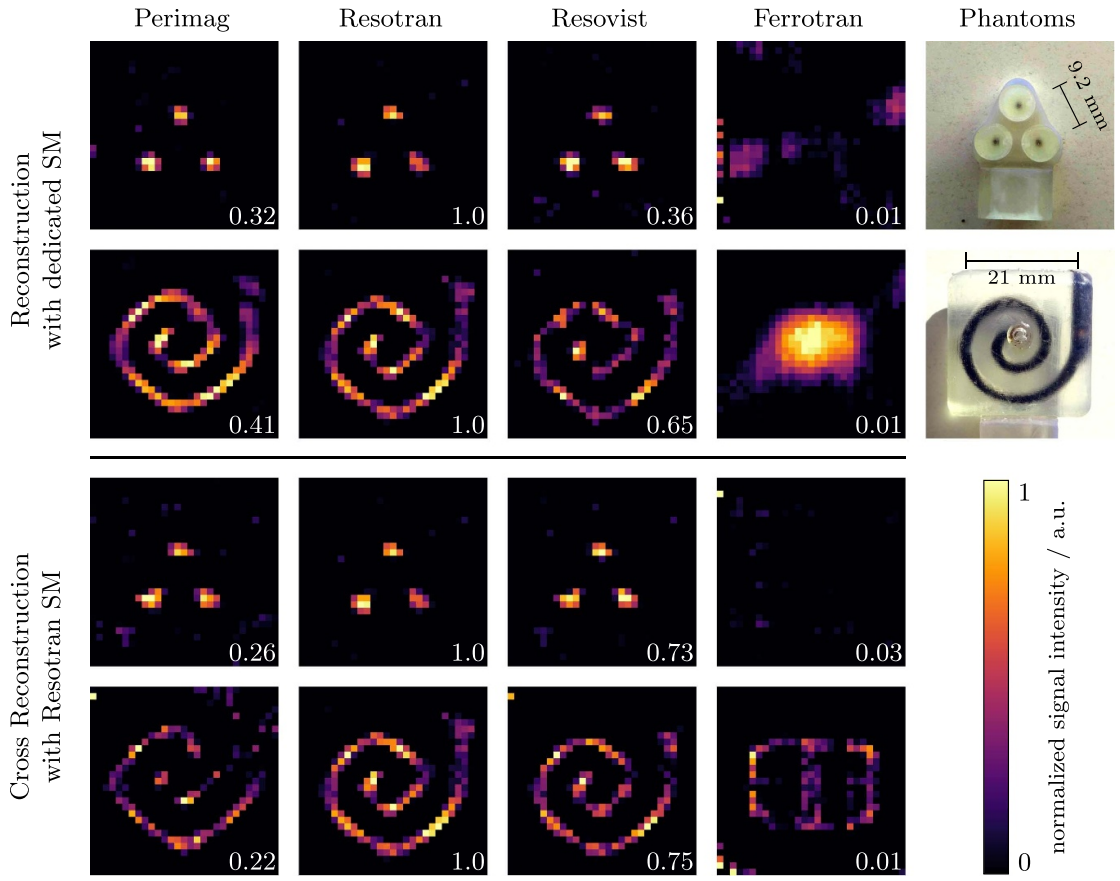

Figure 7. Comparison of MPI reconstructions. Results of the four different MNPs in two different phantoms are shown, each with an iron concentration of 8.5 $mg_{Fe}\,ml^{-1}$. The signal intensity is normalized for each image individually and the reconstructed image has a size of $29 \times 29\,mm^2$. The MPI tailored tracer Perimag provides the best image quality. Resotran and Resovist are similar, but Ferrotran has a very weak particle response. The SSIM to the reconstruction unsing Resotran (row-wise) is superposed in the lower right corner.

for Resovist improves when using the Resotran system matrix. This is supported by the increasing SSIM to the reconstruction of the Resotran spiral (0.75) in comparison to the reconstruction of the spiral using the Resovist system matrix (0.65). One reason may be that there are more disruptions and noise in the Resovist system matrix, as it can be seen in the lowest system matrix component in figure 6. The MNP concentration in the spiral phantom should be consistent, but due to the different representation of the windings by 1 to 3 voxels, the reduced physical resolution towards the edges of the FOV, and the influence of regularization and solver on the reconstruction (Hackelberg *et al* 2024), the intensity seems to vary in the image.

4. Discussion

This work evaluates the four particles Perimag, Resotran, Resovist, and Ferrotran by classifying their sizes, magnetic properties, and imaging performance. We have shown that Resotran and Resovist are similar in composition and performance, with acceptable imaging results, and that Ferrotran is unsuitable for MPI. The reintroduction of ferucarbotran-based MNPs in Germany offers the potential for future human trials in MPI, which motivates a comparison of Resotran with the established but discontinued Resovist.

The purpose of this study is threefold: first, to establish a relationship of the well-known and thoroughly studied MNPs Resovist to the newly MRI approved MNP Resotran, both ferucarbotran, to indicate similar properties and MPI performance. Secondly, this work makes a contribution on the way to an official approval of Resotran for human applications in MPI for vascular imaging based on its similarity to Resovist. Toxicological risks of MNPs on the metabolism remain (Chen *et al* 2010, Singh *et al* 2010, Winer *et al* 2012), however, the long-term application of ferucarbotran in human MRI (Reimer *et al* 1995, Amemiya *et al* 2009) since its introduction in 2003 (Reimer and Balzer 2003) has so far not raised any major concerns (Wang 2011). Third, we complement our study with two more MNPs, one MPI tailored tracer called Perimag to indicate possible future increases in performance and dosage and another called Ferrotran, USPIOs currently in a Phase III study, but not suitable for MPI due to their linear magnetization behavior caused by

their low magnetic energy and their small size. We chose Perimag because it is well studied in the literature (Eberbeck *et al* 2013, Lüdtke-Buzug *et al* 2013, Szwargulski 2020, Ludewig 2022, Vogel *et al* 2023) over a period of 10 years, it appears in various open datasets (Knopp *et al* 2020), its synthesis process is analogous to ferucarbotran and it is expected to perform well in viscous (partially immobilized) media such as blood (Wöckel *et al* 2019, Antonelli *et al* 2020). However, other tracers such as Synomag (Gavilán 2017, Vogel *et al* 2021), VivoTrax (Irfan *et al* 2021b, Gevaert *et al* 2022, Yeo *et al* 2022), PrecisionMRX (Imagion Biosystems Ltd Melbourne, Australia) (Tay *et al* 2017), LS-008 (Vogel 2019), or magnetosomes (Makela *et al* 2022, Thieben *et al* 2023a) have also shown significant potential and even superior magnetic properties for MPI compared to Perimag (Irfan *et al* 2021a, Yeo *et al* 2022).

The size discrepancy of DLS and TEM measurements shows how the hydrodynamic diameter reveals clusters and chains: although Perimag and Ferrotran have similar individual mean core diameters around 3.1 nm (TEM, figure 2), they have very different hydrodynamic diameters (DLS, figure 1), e.g. due to embedded cluster within a single dextran shell for Perimag. Clusters are known to be the MPI active component for signal generation (Eberbeck *et al* 2011) of small MNPs like Perimag and our images show a similar core size of around 5 nm as reported by Eberbeck *et al* (2013). While the short-axis has been considered in our analysis (section 2.3), the long-axis is more relevant to the magnetic properties under investigation. In alignment with the easy axis, particle clusters, chains, and particle-particle interactions play a dominant role in the observed magnetic response in the kHz range (Eberbeck *et al* 2011). However, manual quantification of agglomerates and aggregates (2014) is difficult and prone to user bias and errors in detecting edges and boundaries of overlapping particles (Pyrz and Buttrey 2008, Bresch *et al* 2022). The effective MNP size of Perimag is thus in a range of 20 to 50 nm (visual inspection of figure 2) and these particle ensembles are then surrounded by the dextran shell which yields a hydrodynamic size at around 100 nm as reported in figure 1 by DLS.

Regarding Resovist and Resotran, Gleich and Weizenecker (2005) reported that only 3% of the total iron mass are expected to be MPI active, which agrees with our findings to the extent that the performance of Resotran/Resovist is better than Ferrotran, but worse than Perimag, suggesting that most particle ensembles are too small (Yoshida *et al* 2013). Also, visual inspection of the TEM images reveal small clusters in the 10 to 20 nm range and Resotran/Resovist MNPs overlap much less than Perimag, with a hydrodynamic diameter of about 65 nm. Accordingly, in the case of Ferrotran, the separation by the hull prevents any overlapping particles and particle-particle interactions are suppressed, resulting in MNPs that are too small for MPI with an almost linear magnetization curve in the relevant excitation range. The magnetic properties of Ferrotran indicate that it is not eligible for MPI, which was confirmed with images of poor quality, that do not resemble the measured phantoms in figure 7.

In this study, we did not perform an in-depth analysis regarding the relaxation behavior by blocking Brownian rotation using immobilization methods (Riahi 2020). Regarding Perimag, its third harmonic of a liquid and an immobilized sample have a ratio of $18.31/13.1 \approx 1.4$ (Wöckel *et al* 2019). This ratio indicates a coupled relaxation with a predominant Néel relaxation. From our PSF results, the similarity between Perimag, Resotran and Resovist indicates a similar coupled relaxation behavior. For Ferrotran, almost no relaxation behavior is visible, indicating a fast Néel relaxation, as expected for USPIONs (Krishnan 2010). All four MNPs have similar core sizes around 3 to 4 nm, but very different hydrodynamic diameters with the relationship that the larger the hydrodynamic diameter, the better the MPI performance. A clear distinction in Brownian and Néel relaxation cannot be made on the basis of our results without immobilization. However, our results are analogous to the performance improvement seen due to a larger effective core size as reported by Yoshida *et al* (2013).

The differences in saturation magnetization observed by VSM most likely result from the different material composition ratios for the iron oxides magnetite and maghemite with a saturation magnetization of $98\,\mathrm{Am^2\,kg_{Fe}^{-1}}$ and $82\,\mathrm{Am^2\,kg_{Fe}^{-1}}$, respectively (Colombo *et al* 2012). Additionally, the presence of clusters with particle-particle interaction contribute to a difference in the initial slope of the magnetization curve as indicated by the VSM data in figure 3. Further, VSM successfully predicted the magnetization curve that was measured using MPS, without the hysteresis that is induced by the dynamic excitation field. The center plot of figure 5 confirms this behavior, as the hysteresis curve widens with increasing excitation amplitude and the maximum saturation approaches the values measured with VSM for high amplitudes, without surpassing them. The 1D MPS results are supported by the achieved SNR levels of the measured MPI system matrices and indicate that the imaging quality of the tailored tracer Perimag outperforms all other tracers, which was eventually shown by the reconstruction of the spiral phantom. The analysis of MPS data on tracer performance correlates well with the image reconstructions for all 4 tracers using the system matrix approach. We did not perform *x*-space reconstructions in the time-domain but expect our findings to generalize to other imaging sequences and reconstruction techniques. The FWHM of the *x*-space PSF also

implies a good performance of Perimag and a bad performance of Ferrotran, indicated by a narrow and broad PSF (Croft *et al* 2012), respectively.

Throughout all conducted measurements, the properties and performance of Resovist and Resotran proofed to be akin and the remaining differences could be due to variations between LOT numbers or due to different distributions of the iron oxides magnetite and maghemite. The reconstructed images of figure 7 confirm suitability of Resotran for intricate MPI applications and our work indicates its suitability for 2D sequences, where particle clustering is relevant. On this basis, suitability for more elaborate 3D sequences can be assumed, because the excitation direction is changing for a 2D sequence as well, which is the main difference of 2D/3D excitation to colinear 1D sequences. This is crucial for the medical translation of MPI, although the performance of ferucarbotran-based MNPs does not reach the level of tailored MPI tracers. Cross-reconstructions of Resotran and Resovist are possible, emphasizing their resemblance, and surprisingly even improving the reconstruction result for Resovist using the Resotran system matrix. This might be due to a slightly higher SNR of the Resotran system matrix, as indicated by the analysis in figure 6, similar to the boost in SNR in hybrid system calibration approaches (Von Gladiss *et al* 2017). More investigations on this matter using different particle batches are necessary.

5. Conclusion

Resotran qualifies as a tracer for MPI and its deployment in preclinical trials and system characterizations (Thieben *et al* 2024) could positively impact an official medical approval for MPI. Furthermore, it will facilitate the process of clinical translation of MPI, even if the signal performance is surpassed by tailored MNPs. Due to its similarity to the established MNPs Resovist in both, performance and composition, insights gained on Resovist are in principle transferable to Resotran. With Resovist no longer licensed in most countries, the main benefit of Resotran is the reintroduction of a ferucarbotran-based tracer for medical imaging.

Data availability statement

The data cannot be made publicly available upon publication because they are not available in a format that is sufficiently accessible or reusable by other researchers. The data that support the findings of this study are available upon reasonable request from the authors.

Acknowledgments

This work was supported by the Cluster of Excellence 'CUI: Advanced Imaging of Matter' of the Deutsche Forschungsgemeinschaft (DFG)-EXC 2056-Project ID 390715994. Publishing fees supported by Funding Programme Open Access Publishing of Hamburg University of Technology (TUHH).

Author contributions

A W performed the DLS measurements and carried out the sample preparation for TEM. The TEM measurements were performed by Stefan Werner at the Division of Electron Microscopy of the Chemistry Department at University of Hamburg under the direction of Dr Charlotte Ruhmlieb. J A performed the VSM measurements. F M performed the MPS measurements and analysis. K S measured the dilution series. K S and F M performed the MPI measurements. K S and T K reconstructed the MPI images and did the SNR analysis. T K supervised the project. F M, K S, F W, F T, M A, P V, M G and T K contributed to the conceptualization and theory. F M, K S, J A, A W and F W wrote the original draft. All authors reviewed the final manuscript.

ORCID iDs

Fabian Mohn https://orcid.org/0000-0002-9151-9929
Konrad Scheffler https://orcid.org/0000-0002-6842-9204
Justin Ackers https://orcid.org/0000-0003-1049-0528
Agnes Weimer https://orcid.org/0000-0002-7180-3009
Franz Wegner https://orcid.org/0000-0001-5969-3428
Florian Thieben https://orcid.org/0000-0002-2890-5288
Mandy Ahlborg https://orcid.org/0000-0002-0192-8033
Patrick Vogel https://orcid.org/0000-0003-0801-5146

Matthias Graeser https://orcid.org/0000-0003-1472-5988
Tobias Knopp https://orcid.org/0000-0002-1589-8517

References

Ahlborg M *et al* 2022 First dedicated balloon catheter for magnetic particle imaging *IEEE Trans. Med. Imaging* **41** 3301–8
Amemiya S, Akahane M, Aoki S, Abe O, Kamada K, Saito N and Ohtomo K 2009 Dynamic contrast-enhanced perfusion MR imaging with SPIO: a pilot study *Investigative Radiol.* **44** 503–8
Antonelli A, Szwargulski P, Scarpa E S, Thieben F, Cordula G, Ambrosi G, Guidi L, Ludewig P, Knopp T and Magnani M 2020 Development of long circulating magnetic particle imaging tracers: use of novel magnetic nanoparticles and entrapment into human erythrocytes *Nanomedicine* **15** 739–53
Bakenecker A C, Ahlborg M, Debbeler C, Kaethner C, Buzug T M and Lüdtke-Buzug K 2018 Magnetic particle imaging in vascular medicine *Innov. Surg. Sci.* **3** 179–92
Bakenecker A C, Von Gladiss A, Schwenke H, Behrends A, Friedrich T, Lüdtke-Buzug K, Neumann A, Barkhausen J, Wegner F and Buzug T M 2021 Navigation of a magnetic micro-robot through a cerebral aneurysm phantom with magnetic particle imaging *Sci. Rep.* **11** 14082
Bender P *et al* 2018 Relating magnetic properties and high hyperthermia performance of iron oxide nanoflowers *J. Phys. Chem.* C **122** 3068–77
Billings C, Langley M, Warrington G, Mashali F and Johnson J A 2021 Magnetic particle imaging: current and future applications, magnetic nanoparticle synthesis methods and safety measures *Int. J. Mol. Sci.* **22** 7651
Bresch H, Hodoroaba V-D, Schmidt A, Rasmussen K and Rauscher H 2022 Counting small particles in electron microscopy images—proposal for rules and their application in practice *Nanomaterials* **12** 2238
Bui M P, Le T-A and Yoon J 2021 A magnetic particle imaging-based navigation platform for magnetic nanoparticles using interactive manipulation of a virtual field free point to ensure targeted drug delivery *IEEE Trans. Ind. Electron.* **68** 12493–503
Bui M P, Park M, Le T-A and Yoon J 2023 A development of 3D navigation system for micro-nano robot based on a magnetic particle imaging system *Int. J. Magn. Part. Imaging* **9**
Chandrasekharan P *et al* 2020 Using magnetic particle imaging systems to localize and guide magnetic hyperthermia treatment: tracers, hardware and future medical applications *Theranostics* **10** 2965–81
Chen Y-C, Hsiao J-K, Liu H-M, Lai I-Y, Yao M, Hsu S-C, Ko B-S, Chen Y-C, Yang C-S and Huang D-M 2010 The inhibitory effect of superparamagnetic iron oxide nanoparticle (ferucarbotran) on osteogenic differentiation and its signaling mechanism in human mesenchymal stem cells *Toxicol. Appl. Pharmacol.* **245** 272–9
Colombo M, Carregal-Romero S, Casula M F, Gutiérrez L, Morales M P, Böhm I B, Heverhagen J T, Prosperi D and Parak W J 2012 Biological applications of magnetic nanoparticles *Chem. Soc. Rev.* **41** 4306
Croft L R, Goodwill P, Ferguson M, Krishnan K and Conolly S 2012 Relaxation in x-space magnetic particle imaging *Springer Proc. Phys.* **140** 149–53
Deissler R J, Wu Y and Martens M A 2014 Dependence of Brownian and Néel relaxation times on magnetic field strength *Med. Phys.* **41** 012301
Dittmer S, Kluth T, Henriksen M T R and Maass P 2021 Deep image prior for 3D magnetic particle imaging: a quantitative comparison of regularization techniques on open MPI dataset *Int. J. Magn. Part. Imaging* **7**
Eberbeck D, Dennis C L, Huls N F, Krycka K L, Gruttner C and Westphal F 2013 Multicore magnetic nanoparticles for magnetic particle imaging *IEEE Trans. Magn.* **49** 269–74
Eberbeck D, Wiekhorst F, Wagner S and Trahms L 2011 How the size distribution of magnetic nanoparticles determines their magnetic particle imaging performance *Appl. Phys. Lett.* **98** 182502
Ferguson R M *et al* 2015 Magnetic particle imaging with tailored iron oxide nanoparticle tracers *IEEE Trans. Med. Imaging* **34** 1077–84
Ferguson R M, Minard K R and Krishnan K M 2009 Optimization of nanoparticle core size for magnetic particle imaging *J. Magn. Magn. Mater.* **321** 1548–51
Foner S 1959 Versatile and sensitive vibrating-sample magnetometer *Rev. Sci. Instrum.* **30** 548–57
Franke J, Heinen U, Lehr H, Weber A, Jaspard F, Ruhm W, Heidenreich M and Schulz V 2016 System characterization of a highly integrated preclinical hybrid MPI-MRI scanner *IEEE Trans. Med. Imaging* **35** 1993–2004
Gavilán H *et al* 2017 Colloidal flower-shaped iron oxide nanoparticles: synthesis strategies and coatings *Part. Part. Syst. Charact.* **34** 1700094
Gevaert J, Van Beek K, Sehl O C and Foster P J 2022 VivoTrax+ improves the detection of cancer cells with magnetic particle imaging *Int. J. Magn. Part. Imaging* **8**
Gleich B and Weizenecker J 2005 Tomographic imaging using the nonlinear response of magnetic particles *Nature* **435** 1214–7
Goodwill P W, Lu K, Zheng B and Conolly S M 2012 An X-space magnetic particle imaging scanner *Rev. Sci. Instrum.* **83** 33708–9
Graeser M *et al* 2019 Human-sized magnetic particle imaging for brain applications *Nat. Commun.* **10** 1936
Graeser M, Knopp T, Szwargulski P, Friedrich T, Von Gladiss A, Kaul M, Krishnan K M, Ittrich H, Adam G and Buzug T M 2017 Towards picogram detection of superparamagnetic iron-oxide particles using a gradiometric receive coil *Sci. Rep.* **7** 6872
Hackelberg N, Grosser M, Tsanda A, Mohn F, Scheffler K, Möddel M and Knopp T 2024 RegularizedLeastSquares.jl: modality agnostic Julia package for solving regularized least squares problems *Int. J. Magn. Part. Imaging* **10**
Hackelberg N, Schumacher J, Ackers J, Möddel M, Förger F, Graeser M and Knopp T 2023 MPIMeasurements.Jl: an extensible julia framework for composable magnetic particle imaging devices *Int. J. Magn. Part. Imaging* **9**
Hackelberg N, Schumacher J, Graeser M and Knopp T 2022 A flexible high-performance signal generation and digitization plattform based on low-cost hardware *Int. J. Magn. Part. Imaging* **8**
Haegele J *et al* 2016a Magnetic particle imaging: a resovist based marking technology for guide wires and catheters for vascular interventions *IEEE Trans. Med. Imaging* **35** 2312–8
Haegele J, Rahmer J, Gleich B, Borgert J, Wojtczyk H, Panagiotopoulos N, Buzug T M, Barkhausen J and Vogt F M 2012 Magnetic particle imaging: visualization of instruments for cardiovascular intervention *Radiology* **265** 933–8
Haegele J, Vaalma S, Panagiotopoulos N, Barkhausen J, Vogt F M, Borgert J and Rahmer J 2016b Multi-color magnetic particle imaging for cardiovascular interventions *Phys. Med. Biol.* **61** N415–26
Hartung V, Günther J, Augustin A M, Reichl T, Gruschwitz P, Rückert M, Bley T A, Behr V, Herz S and Vogel P 2023 Resotran® meets MPI—clinically approved ferucarbotran reintroduced: a major leap towards MPI in humans *Int. J. Magn. Part. Imaging* **9**

Harvell-Smith S, Tung L D and Thanh N T K 2022 Magnetic particle imaging: tracer development and the biomedical applications of a radiation-free, sensitive and quantitative imaging modality *Nanoscale* **14** 3658–97
He J, Li Y, Zhu T, Zhong J, Hui H and Tian J 2023 Simulation study of a magnetic particle imaging device capable of hyperthermia *Int. J. Magn. Part. Imaging* **9**
Herz S, Vogel P, Kampf T, Dietrich P, Veldhoen S, Rückert M A, Kickuth R, Behr V C and Bley T A 2019 Magnetic particle imaging–guided stenting *J. Endovasc. Ther.* **26** 512–9
Irfan M, Dogan N, Bingolbali A and Aliew F 2021b Synthesis and characterization of $NiFe_2O_4$ magnetic nanoparticles with different coating materials for magnetic particle imaging (MPI) *J. Magn. Magn. Mater.* **537** 168150
Irfan M, Dogan N, Sapmaz T and Bingolbali A 2021a Development of MPI relaxometer for characterization of superparamagnetic nanoparticles *J. Magn. Magn. Mater.* **536** 168082
ISO 13322-1 2014 *Static Image Analysis Methods* (International Organisation for Standardization)
Kaul M G, Salamon J, Knopp T, Ittrich H, Adam G, Weller H and Jung C 2018 Magnetic particle imaging for *in vivo* blood flow velocity measurements in mice *Phys. Med. Biol.* **63** 64001
Knopp T, Gdaniec N and Möddel M 2017 Magnetic particle imaging: from proof of principle to preclinical applications *Phys. Med. Biol.* **62** R124–78
Knopp T, Szwargulski P, Griese F and Gräser M 2020 OpenMPIData: an initiative for freely accessible magnetic particle imaging data *Data Brief* **28** 104971
Koppel D E 1972 Analysis of macromolecular polydispersity in intensity correlation spectroscopy: the method of cumulants *J. Chem. Phys.* **57** 4814–20
Krishnan K M 2010 Biomedical nanomagnetics: a spin through possibilities in imaging, diagnostics and therapy *IEEE Trans. Magn.* **46** 2523–58
Löwa N, Gutkelch D, Welge E-A, Welz R, Meier F, Baki A, Bleul R, Klein T and Wiekhorst F 2020 Novel benchtop magnetic particle spectrometer for process monitoring of magnetic nanoparticle synthesis *Nanomaterials* **10** 2277
Löwa N, Radon P, Kosch O and Wiekhorst F 2016 Concentration dependent MPI tracer performance *Int. J. Magn. Part. Imaging* **2** 1–5
Lüdtke-Buzug K, Haegele J, Biederer S, Sattel T F, Erbe M, Duschka R L, Barkhausen J and Vogt F M 2013 Comparison of commercial iron oxide-based MRI contrast agents with synthesized high-performance MPI tracers *Biomed. Tech.* **58** 527–33
Liu S, Chiu-Lam A, Rivera-Rodriguez A, DeGroff R, Savliwala S, Sarna N and Rinaldi-Ramos C M 2021 Long circulating tracer tailored for magnetic particle imaging *Nanotheranostics* **5** 348–61
Lu K, Goodwill P W, Saritas E U, Zheng B and Conolly S M 2013 Linearity and shift invariance for quantitative magnetic particle imaging *IEEE Trans. Med. Imaging* **32** 1565–75
Ludewig P *et al* 2017 Magnetic particle imaging for real-time perfusion imaging in acute stroke *ACS Nano* **11** 10480–8
Ludewig P *et al* 2022 Magnetic particle imaging for assessment of cerebral perfusion and ischemia *Wiley Interdiscip. Rev.-Nanomed. Nanobiotechnol.* **14** e1757
Ludwig F, Eberbeck D, Löwa N, Steinhoff U, Wawrzik T, Schilling M and Trahms L 2013 Characterization of magnetic nanoparticle systems with respect to their magnetic particle imaging performance *Biomed. Tech./Biomed. Eng.* **58**
Makela A V, Schott M A, Madsen C S, Greeson E M and Contag C H 2022 Magnetic particle imaging of magnetotactic bacteria as living contrast agents is improved by altering magnetosome arrangement *Nano Lett.* **22** 4630–9
Mason E E, Cooley C Z, Cauley S F, Griswold M A, Conolly S M and Wald L L 2017 Design analysis of an MPI human functional brain scanner *Int. J. Magn. Part. Imaging* **3**
Mattingly E, Śliwiak M, Drago J, Mason E, Graeser M and Wald L 2022 A drive filter design for MPI with harmonic notching and selective damping *Int. J. Magn. Part. Imaging* **8**
Mohn F, Exner M, Szwargulski P, Möddel M, Knopp T and Graeser M 2023 Saline bolus for negative contrast perfusion imaging in magnetic particle imaging *Phys. Med. Biol.* **68** 175026
Mohn F, Knopp T, Boberg M, Thieben F, Szwargulski P and Graeser M 2022 System matrix based reconstruction for pulsed sequences in magnetic particle imaging *IEEE Trans. Med. Imaging* **41** 1862–73
Moor L, Scheibler S, Gerken L, Scheffler K, Thieben F, Knopp T, Herrmann I K and Starsich F H L 2022 Particle interactions and their effect on magnetic particle spectroscopy and imaging *Nanoscale* **14** 7163–73
Neumann A *et al* 2022 Recent developments in magnetic particle imaging *J. Magn. Magn. Mater.* **550** 169037
Ozaslan A A, Utkur M, Canpolat U, Tuncer M A, Karli Oguz K and Saritas E U 2022 PNS limits for human head-size MPI systems: preliminary results *Int. J. Magn. Part. Imaging* **8**
Pyrz W D and Buttrey D J 2008 Particle size determination using TEM: a discussion of image acquisition and analysis for the novice microscopist *Langmuir* **24** 11350–60
Rahmer J, Stehning C and Gleich B 2018 Remote magnetic actuation using a clinical scale system *PLoS One* **13** e0193546
Reimer P and Balzer T 2003 Ferucarbotran (Resovist): a new clinically approved res-specific contrast agent for contrast-enhanced MRI of the liver: properties, clinical development and applications *Eur. Radiol.* **13** 1266–76
Reimer P, Schuierer G, Balzer T and Peters P E 1995 Application of a superparamagnetic iron oxide (Resovis®) for MR imaging of human cerebral blood volume *Magn. Reson. Med.* **34** 694–7
Remmo A, Löwa N, Kosch O, Eberbeck D, Ludwig A, Kampen L, Grüttner C and Wiekhorst F 2022 Cell tracking by magnetic particle imaging: methodology for labeling THP-1 monocytes with magnetic nanoparticles for cellular imaging *Cells* **11** 2892
Riahi K *et al* 2020 Magnetic performance of Synomag® nanoparticles in various environments *Int. J. Magn. Part. Imaging* **6**
Rubia-Rodriguez I *et al* 2021 Whither magnetic hyperthermia? A tentative roadmap *Materials* **14** 706
Saritas E U, Goodwill P W, Zhang G Z and Conolly S M 2013 Magnetostimulation limits in magnetic particle imaging *IEEE Trans. Med. Imaging* **32** 1600–10
Sattel T F, Woywode O, Weizenecker J, Rahmer J, Gleich B and Borgert J 2015 Setup and validation of an MPI signal chain for a drive field frequency of 150 kHz *IEEE Trans. Magn.* **51** 1–3
Scheffler K, Boberg M and Knopp T 2024 Solving the MPI reconstruction problem with automatically tuned regularization parameters *Phys. Med. Biol.* **69** 045024
Scheffler K, Thieben F, Mohn F, Graeser M and Knopp T 2023 MPI signal performance of Resotran *12th Int. Workshop on Magnetic Particle Imaging (IWMPI 2023)* vol 9 p 1
Schmale I *et al* 2013 Human PNS and SAR study in the frequency range from 24 to 162 kHz *2013 Int. Workshop on Magnetic Particle Imaging, IWMPI 2013* p 1
Sehl O C, Gevaert J J, Melo K P, Knier N N and Foster P J 2020 A perspective on cell tracking with magnetic particle imaging *Tomography* **6** 315–24

Singh N, Jenkins G J S, Asadi R and Doak S H 2010 Potential toxicity of superparamagnetic iron oxide nanoparticles (SPION) *Nano Rev.* **1** 5358
Song G, Chen M, Zhang Y, Cui L, Qu H, Zheng X, Wintermark M, Liu Z and Rao J 2018 Janus iron oxides @ semiconducting polymer nanoparticle tracer for cell tracking by magnetic particle imaging *Nano Lett.* **18** 182–9
Sun C, Lee J S H and Zhang M 2008 Magnetic nanoparticles in MR imaging and drug delivery *Adv. Drug. Deliv. Rev.* **60** 1252–65
Szwargulski P *et al* 2020 Monitoring intracranial cerebral hemorrhage using multicontrast real-time magnetic particle imaging *ACS Nano* **14** 13913–23
Tay Z W *et al* 2021 Superferromagnetic nanoparticles enable order-of-magnitude resolution & sensitivity gain in magnetic particle imaging *Small Methods* **5** 2100796
Tay Z W, Goodwill P W, Hensley D W, Taylor L A, Zheng B and Conolly S M 2016 A high-throughput, arbitrary-waveform, MPI spectrometer and relaxometer for comprehensive magnetic particle optimization and characterization *Sci. Rep.* **6** 34180
Tay Z W, Hensley D W, Vreeland E C, Zheng B and Conolly S M 2017 The relaxation wall: experimental limits to improving MPI spatial resolution by increasing nanoparticle core size *Biomed. Phys. Eng. Express* **3** 035003
Thieben F, Foerger F, Mohn F, Hackelberg N, Boberg M, Scheel J-P, Möddel M, Graeser M and Knopp T 2024 System characterization of a human-sized 3D real-time magnetic particle imaging scanner for cerebral applications *Commun. Eng.* **3** 47
Thieben F, Knopp T, Boberg M, Foerger F, Graeser M and Moddel M 2023b On the receive path calibration of magnetic particle imaging systems *IEEE Trans. Instrum. Meas.* **72** 1–15
Thieben F, Mickoleit F, Tessaro S, Ludewig P, Schüler D, Garbayo J R, Uebe R and Knopp T 2023a Development of optimized magnetic particle imaging tracers utilizing genetically engineered magnetosomes *Int. J. Magn. Part. Imaging* **9**
Thomas J C 1987 The determination of log normal particle size distributions by dynamic light scattering *J. Colloid Interface Sci.* **117** 187–92
Verleysen E, Wagner T, Lipinski H-G, Kägi R, Koeber R, Boix-Sanfeliu A, De Temmerman P-J and Mast J 2019 Evaluation of a TEM based approach for size measurement of particulate (nano)materials *Materials* **12** 2274
Vogel P *et al* 2019 Micro-traveling wave magnetic particle imaging—sub-millimeter resolution with optimized tracer LS-008 *IEEE Trans. Magn.* **55** 1–7
Vogel P, Kampf T, Rückert M, Grüttner C, Kowalski A, Teller H and Behr V 2021 Synomag®: the new high-performance tracer for magnetic particle imaging *Int. J. Magn. Part. Imaging* **7**
Vogel P, Rückert M A, Greiner C, Günther J, Reichl T, Kampf T, Bley T A, Behr V C and Herz S 2023 iMPI: portable human-sized magnetic particle imaging scanner for real-time endovascular interventions *Sci. Rep.* **13** 10472
Von Gladiss A, Graeser M, Szwargulski P, Knopp T and Buzug T M 2017 Hybrid system calibration for multidimensional magnetic particle imaging *Phys. Med. Biol.* **62** 3392–406
Wöckel L, Wells J, Kosch O, Lyer S, Alexiou C, Grüttner C, Wiekhorst F and Dutz S 2019 Long-term stable measurement phantoms for magnetic particle imaging *J. Magn. Magn. Mater.* **471** 1–7
Wang Y-X J 2011 Superparamagnetic iron oxide based MRI contrast agents: current status of clinical application *Quant. Imaging Med. Surg.* **1** 35–40
Wang Z, Bovik A C, Sheikh H R and Simoncelli E P 2004 Image quality assessment: from error visibility to structural similarity *IEEE Trans. Image Process.* **13** 600–12
Wegner F *et al* 2021 Magnetic particle imaging: in vitro signal analysis and lumen quantification of 21 endovascular stents *Int. J. Nanomed.* **ume 16** 213–21
Weizenecker J, Borgert J and Gleich B 2007 A simulation study on the resolution and sensitivity of magnetic particle imaging *Phys. Med. Biol.* **52** 6363–74
Weizenecker J, Gleich B, Rahmer J, Dahnke H and Borgert J 2009 Three-dimensional real-time *in vivo* magnetic particle imaging *Phys. Med. Biol.* **54** L1–L10
Winer J L, Liu C Y and Apuzzo M L J 2012 The use of nanoparticles as contrast media in neuroimaging: a statement on toxicity *World Neurosurg.* **78** 709–11
Yang X, Shao G, Zhang Y, Wang W, Qi Y, Han S and Li H 2022 Applications of magnetic particle imaging in biomedicine: advancements and prospects *Front. Physiol.* **13** 898426
Yeo K H, Rodrigo I, Kuo R, Chandrasekharan P, Fellows B and Conolly S 2022 Characterizing the performance of commercial magnetic particles for magnetic particle imaging *Int. J. Magn. Part. Imaging* **8**
Yoshida T, Othman N B and Enpuku K 2013 Characterization of magnetically fractionated magnetic nanoparticles for magnetic particle imaging *J. Appl. Phys.* **114** 173908
Zheng B, Vazin T, Goodwill P W, Conway A, Verma A, Ulku Saritas E, Schaffer D and Conolly S M 2015 Magnetic particle imaging tracks the long-term fate of *in vivo* neural cell implants with high image contrast *Sci. Rep.* **5** 14055